Proceedings of the Combustion Institute 40 (2024) 105665

Contents lists available at ScienceDirect

Proceedings of the Combustion Institute

journal homepage: www.elsevier.com/locate/proci

The role of thermodiffusion and dimensionality in the formation of cellular instabilities in hydrogen flames

Thorsten Zirwes [a,*], Feichi Zhang [b], Thomas L. Kaiser [c], Kilian Oberleithner [c], Oliver T. Stein [d], Henning Bockhorn [d], Andreas Kronenburg [a]

[a] Institute for Combustion Technology (ITV), University of Stuttgart, Pfaffenwaldring 31, 70569 Stuttgart, Germany
[b] Institute for Technical Chemistry, Karlsruhe Institute of Technology, Kaiserstr.12, 76131, Karlsruhe, Germany
[c] Laboratory for Flow Instabilities and Dynamics, Institute of Fluid Dynamics and Technical Acoustics, Technische Universität Berlin, Müller-Breslau-Straße 8, 10623 Berlin, Germany
[d] Engler-Bunte Institute, Karlsruhe Institute of Technology, Engler-Bunte-Ring 7, 76131 Karlsruhe, Germany

ARTICLE INFO

Keywords:
Hydrogen combustion
Cellular instabilities
Resolved numerical simulations
Soret diffusion
Laminar flames

ABSTRACT

Hydrogen is quickly becoming one of the most important fuels for combustion applications. However, compared to conventional hydro-carbon flames, the high diffusivity of hydrogen makes lean hydrogen flames prone to form cellular instabilities. In this work, the formation of cellular structures on a lean hydrogen–air flame is studied numerically in a laminar flow with prescribed initial perturbation. The flame is fully resolved and a detailed reaction mechanism as well as detailed diffusion models are utilized. In the literature, most numerical works directly studying cell formation are limited to two-dimensional setups. However, the additional principal curvature direction in three dimensions can have a strong impact on the cell formation and flame propagation. Because of this, simulations are performed both in 2D and 3D to directly quantify the effect of dimensionality on flame propagation. In the 3D simulations, higher local curvatures yield local heat release rates that exceed the ones from 2D simulations by 80%. In addition, simulations with and without thermo or Soret diffusion are carried out. While Soret diffusion leads to a decrease in flame speed for freely propagating flames, it accelerates the formation of thermodiffusively unstable cells as well as increases local heat release rates. This can be explained by an increase of local equivalence ratios in the reaction and post-oxidation zone due to the altered focusing of diffusive fluxes, leading to locally increased heat release rates for positively curved flame segments. The efficiency factor I is evaluated to model the effect of the cellular structures on the local burning rate. I increases during the formation of primary cells and reaches a quasi-steady value once the secondary structures are formed, which can present an approach for modeling the effect of cellular structures on hydrogen flame dynamics.

1. Introduction

The current transition towards sustainable energy requires a shift from carbon-based fossil fuels to hydrogen-based fuels produced from renewable sources. However, because hydrogen has a much higher diffusivity than conventional hydrocarbon fuels, hydrogen flames are prone to intrinsic thermodiffusive instabilities [1–4]. Especially in lean mixtures of hydrogen and air, characteristic cellular structures appear on the flame's surface because of the local imbalance of fuel, oxidizer and heat diffusion. The cellular structures are characterized by strong negative flame stretch in the cusps that can lead to local extinction [5,6], also observable as tip opening in laminar flames [7,8], and positive curvatures with local flame speed enhancement at the leading points. Although these cellular structures strongly affect the local flame structure and are important for the overall flame propagation, they remain challenging to model due to their complex dependence on the local flame stretch and small size, which can be below the subgrid cutoff length.

The occurrence of cellular instabilities has been well documented experimentally in the literature, especially for (high-pressure) spherically expanding flames [9,10]. An in-depth numerical study of these structures requires the use of high-fidelity simulations that fully resolve the flame front. Because of this, simulations targeting thermodiffusive instabilities are computationally expensive, so that previous studies of this effect for laminar cases are based on 2D simulations [11]. Recently, Berger et al. [12] isolated the effect of Darrieus–Landau and thermodiffusive instabilities on cell formation. They also derived dispersion relations for the cell growths [2], which were further analyzed

* Corresponding author.
E-mail address: thorsten.zirwes@itv.uni-stuttgart.de (T. Zirwes).

https://doi.org/10.1016/j.proci.2024.105665
Received 4 December 2023; Accepted 10 July 2024
Available online 3 August 2024

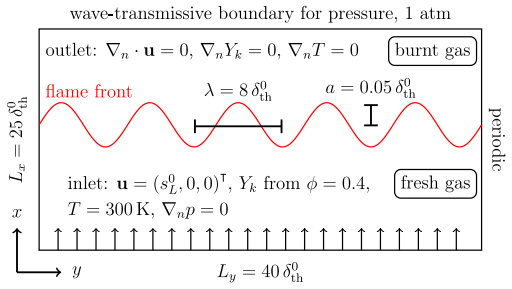

Fig. 1. Computational setup and boundary conditions.

by Gaucherand et al. [13]. Wen et al. [14,15] investigated flamelet approaches to model the structure of the cells. Eckart et al. [16] studied the effect of CO_2 addition to hydrogen flames and found an increased propensity to form cellular instabilities. While these studies yield useful insights into cell formation, performing the simulations in two dimensions means that the cells only have one principal curvature direction, which limits how strongly diffusion fluxes can be focused or defocused. While three-dimensional simulations of hydrogen-based flames can be found in the literature [17–19], they are almost exclusively performed in turbulent flows, which makes an isolated investigation of cellular instabilities more difficult due to the interaction of the cellular structures with the turbulent flow. Patyal and Matalon [20,21] showed that instability growth due to the Darrieus–Landau instability is faster in 3D compared to 2D. However, their study explicitly did not assess thermodiffusive instabilities. Aspden et al. [22] compared laminar and turbulent flame statistics arising from thermodiffusively unstable hydrogen flames. Subsequently, Howarth et al. [23] studied thermodiffusive instabilities in turbulent flows and highlighted the importance of leading points for flame propagation. Howarth and Aspden [24] evaluated PDFs of local flame speed and curvature of thermodiffusively unstable hydrogen flames at elevated pressure and determined efficiency factors.

In this work we provide fully resolved numerical simulations of a thermodiffusively unstable hydrogen flame, both in two and three dimensions, to evaluate local and global differences in the propagation speed, cell formation and flame structure. Since the instability is driven by Lewis number effects and preferential diffusion, molecular diffusion fluxes must be considered in detail. One interesting aspect of hydrogen flames is the importance of Soret or thermodiffusion. However, detailed studies on the influence of the Soret effect on the formation of cellular instabilities is currently not available. Grcar et al. [25] compared the impact of using multi-component diffusion instead of mixture-averaged diffusion on local chemical pathways. Recently, Schlup and Blanquart [26] performed 2D and 3D simulations with and without Soret diffusion. They found that the Chapman and Cowling model for Soret diffusion agrees well with the full multicomponent model. To provide further insight into the effect of Soret diffusion on cell formation, we perform simulations in this work where Soret diffusion is disabled to provide a direct quantitative comparison.

Two computational setups are considered, a 2D Cartesian rectangle and a 3D box domain with inlets providing a laminar homogeneous inflow of the premixed hydrogen–air mixture at atmospheric and lean conditions. A detailed reaction mechanism is used together with detailed diffusion models.

2. Computational setup

The computational setup for the simulations performed in 2D follows the general setup of Berger et al. [3] and consists of a rectangular domain with side lengths $L_x \times L_y = 25\,\delta^0_{\mathrm{th}} \times 40\,\delta^0_{\mathrm{th}}$, where δ^0_{th} is the thermal thickness $\delta^0_{\mathrm{th}} = (\max(T) - \min(T))/\max(|\nabla T|)$ of the corresponding 1D freely-propagating flame (FPF). These dimensions correspond to one fully developed flame finger [3]. The reference time is computed from $\tau = \delta^0_{\mathrm{th}}/s^0_L$ (see Table 1). For the 3D simulations, the domain is extended in the z direction with $L_z = L_y$. The supplementary material contains additional validation of the independence of the simulation results from the domain size.

Table 1
Properties of reference laminar 1D flames.

ϕ	Soret	s^0_L (m/s)	δ^0_{th} (mm)	τ (ms)	$Y_{\mathrm{H_2,iso}}$
0.4	no	0.239	0.599	2.510	0.00138
0.4	yes	0.227	0.613	2.703	0.00128

The simulation domain is depicted in Fig. 1. Unburnt premixed gas enters the domain with a block flow profile from the inlet at the bottom. The flow speed is set to s^0_L, which is the flame speed of the corresponding 1D freely propagating, unstretched flame. The mixture composition is set to an equivalence ratio of $\phi = 0.4$ for H_2-air and the temperature of the unburnt gas is $T = 300\,\mathrm{K}$. At the outlet, zero gradient conditions are prescribed for species mass fractions Y_k, velocity and temperature. In the y-direction, periodic boundary conditions are chosen.

To start the formation of cellular instabilities in a controlled manner, the initial conditions for T, Y_k and $\vec{u}$ are set according to the corresponding 1D freely-propagating flame solution but perturbed with a prescribed wavelength and amplitude. In this work, the fields of solution variables $\vec{\theta} = \{T, Y_k, u_x\}$ are initially set according to

$$\vec{\theta}(x, y, z) = \vec{\theta}^0 \left(x^0 + a \sin\left(\frac{2\pi y}{\lambda}\right) \sin\left(\frac{2\pi z}{\lambda}\right) \right). \tag{1}$$

where x and y are the global coordinates, x^0 are the coordinates of the 1D freely-propagating flame, $\lambda = 8\delta_{\mathrm{th}}$ is the wave length of the initial perturbation corresponding to a fast-growing wave number [3], and $\vec{\theta}^0(x^0)$ is the solution of the 1D freely propagating flame. In this way, any line at constant y corresponds to the 1D flame solution. For the 2D simulations, the last term in Eq. (1) is omitted, which corresponds to setting $z = 0.25\lambda$. For the 3D simulations, the computational domain is extended in the z-direction with a total size of $L_x \times L_y \times L_z = 25\,\delta^0_{\mathrm{th}} \times 40\,\delta^0_{\mathrm{th}} \times 40\,\delta^0_{\mathrm{th}}$ and periodic boundaries in the z-direction.

The simulations are performed with the in-house code `EBIdnsFOAM` [27], which uses the finite volume method to solve the fully compressible Navier–Stokes equations. The code uses Cantera to provide detailed diffusion coefficients for each species. The finite rate chemistry model is employed to compute the chemical reaction rates based on the detailed hydrogen–air reaction mechanism by Li et al. [28], which contains 9 species and 21 chemical reactions. To ensure the full resolution of the flame, the computational grid resolution is equidistantly set to $\Delta_x = \Delta_y = \delta^0_{\mathrm{th}}/20$. Simulations with $\delta^0_{\mathrm{th}}/40$ have been carried out to validate the grid resolution. Simulations with $\delta^0_{\mathrm{th}}/20$ and $\delta^0_{\mathrm{th}}/40$ lead to slightly different secondary cell structures, which is expected due to the nature of the instability, which is very sensitive to the initial flame evolution. However, both $\delta^0_{\mathrm{th}}/20$ and $\delta^0_{\mathrm{th}}/40$ predict the same flame structure, with differences in maximum heat release rates of about 5%. To directly compare the 2D and 3D simulations, all presented results are obtained from the mesh with $\delta^0_{\mathrm{th}}/20$. All spatial derivatives are discretized by fourth order interpolation schemes and an implicit second order backward scheme is used for temporal discretization. The mixture-averaged diffusion model (Curtiss–Hischfelder approximation) [29] is used together with detailed Soret diffusion [26].

3. Formation of cellular structures

Fig. 2 presents the temporal evolution of the flame front from the 3D simulation, shown as an iso-surface of $Y_{\mathrm{H_2,iso}}$, which is the hydrogen mass fraction at the maximum heat release rate of the reference 1D flame (see Table 1). The snapshots are given at different times t normalized by the flame transit time of the 1D reference flames τ. At $t/\tau = 0$, the initial perturbation is visible. Until $t/\tau = 3.5$, primary

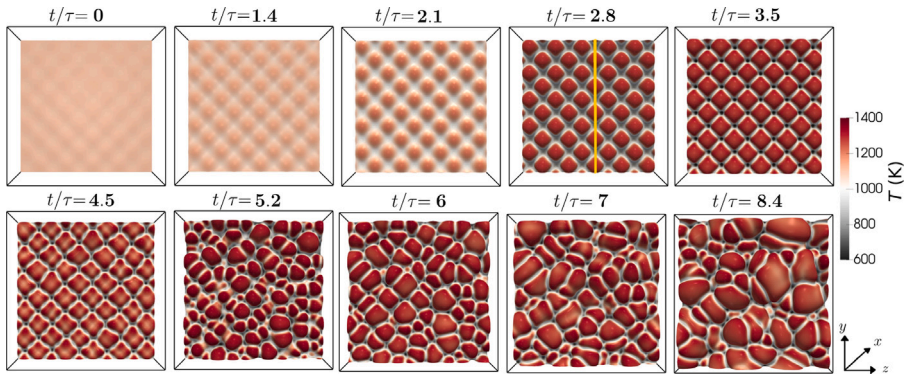

Fig. 2. Iso-surface of $Y_{H_{2,iso}}$ at different times colored by temperature T, looking in the positive x direction (outlet at the back, inlet at the front) for hydrogen–air at $\phi = 0.4$ including Soret diffusion.

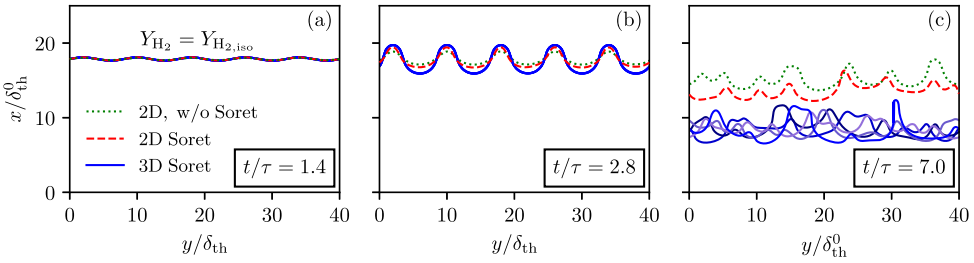

Fig. 3. Iso-lines of $Y_{H_{2,iso}}$ from the 2D simulation without Soret diffusion (green dotted line), from the 2D simulation including Soret diffusion (red dashed line) and from the 3D simulation including Soret diffusion (iso-lines obtained from slices through the iso-surface at $z = (n + 0.25)\lambda$, $n = 1 \dots 5$, one of which is indicated in Fig. 2) at three different normalized times t/τ.

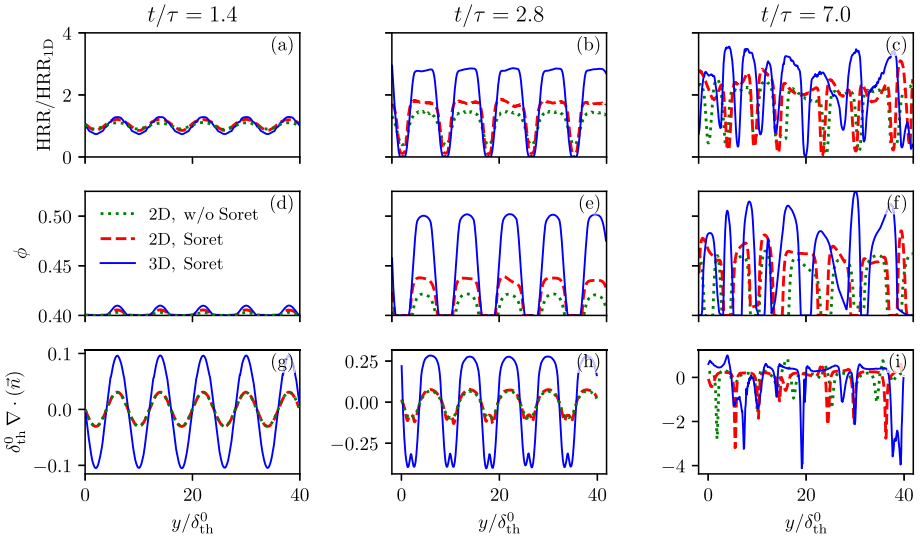

Fig. 4. Maximum heat release rate HRR normalized by the corresponding maximum heat release rate from the 1D reference flames as a function of y (top row), local equivalence ratio ϕ at the position of maximum HRR (center row) and normalized curvature at the maximum HRR (bottom row) presented at three different time instances.

cellular structures form in a symmetric way. Beginning with $t/\tau = 4.5$, the primary cellular structures collapse into secondary structures. It should be noted that this cell growth is mainly attributed to the thermodiffusive instability. An extended discussion can be found in the supplementary material.

Fig. 3 presents a more detailed view of the formation process. Three time instances are chosen: $t/\tau = 1.4$ (Fig. 3a), where the flames are close to the initial perturbation; $t/\tau = 2.8$ (Fig. 3b), which represents the structure of the primary cells; and $t/\tau = 7$ (Fig. 3c), which lies well within the secondary cell formation regime. For the 2D simulations, the dashed and dotted lines in the figure represent the iso-line of $Y_{H_{2,iso}}$, whereas the flame front from the 3D simulation is represented by five axial cuts through the flame front, one of which is shown in Fig. 2 at $t/\tau = 2.8$ as yellow line. At $t/\tau = 1.4$ (Fig. 3c), the location of the flame front from all three cases (full 3D simulation with Soret diffusion, blue solid line; 2D simulation with Soret diffusion, red dashed line; 2D simulation without Soret diffusion; green dotted line) overlap. At $t/\tau = 2.8$ (Fig. 3b), after the primary structures had time to develop, the cellular structures in the 3D simulation have grown the most (note that all five iso-lines from the 3D simulation overlap due to the symmetric structure of the cells), while the cells from the 2D simulation without Soret diffusion have grown the least. This trend continues for the secondary structures as well at $t/\tau = 7$ (Fig. 3c), where the flame from

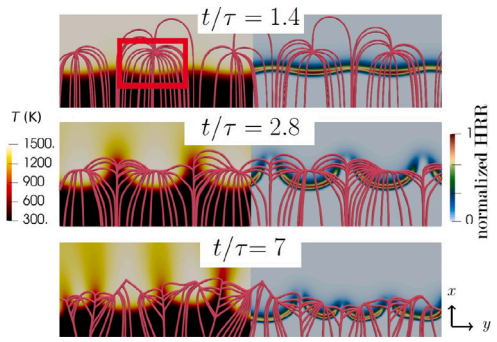

Fig. 5. Temperature field (left) and HRR (right) at three different time instances shown together with trajectories (red lines) of reaction progress c from the 2D simulation with Soret diffusion.

the 3D simulation has propagated the furthest, while the 2D simulation without Soret diffusion lags behind.

The different propagation velocities can be explained by the results in Fig. 4. The top row presents the maximum heat release rate along each y-coordinate of the 2D simulation and the yellow line marked in Fig. 2 for the 3D simulation at the three different time instances. The second row shows the maximum of the local equivalence ratio ϕ along each y coordinate, which are further analyzed in the next section. The third row presents the normalized flame front curvature at the position of the maximum heat release rate. Even though the flames at $t/\tau = 1.4$ have the same shape (Fig. 3a), the local heat release rates are enhanced for the 3D case (Fig. 4a). The reason for this is shown in Figs. 4b and c: even though the shape of the flame is the same in the 2D cutting plane, the flame front curvature in 3D is higher than in 2D. The curvature-induced enhancement of diffusive fluxes thus leads to higher local equivalence ratios at the positively curved flame segments. Note that the two 2D cases have the same curvatures, but local heat release rates are slightly enhanced for the 2D case with Soret diffusion (see the next section for further discussion). At $t/\tau = 2.8$ (Fig. 4b), heat release rates at the positively curved part of the flame are 80% larger in 3D compared to the same time instance of the 2D case. Again, the higher curvatures in 3D (Fig. 4h) lead to the higher local equivalence ratios (Fig. 4e), causing this difference in heat release rates and thus propagation speeds. PDFs of local equivalence ratio and curvature across the whole flame front for $t/\tau = 2.8$ are provided as supplementary material. For the secondary cells (Fig. 4c, f, i), this trend continues with the highest local heat release rates and equivalence ratios found in the 3D case.

4. Effect of soret diffusion

For the 1D unstretched flames, including the Soret diffusion leads to a slight decrease of the laminar flame speed (see e.g. s_L^0 in Table 1). However, during the cell formation, the 2D simulation with Soret diffusion exhibits larger propagation speeds and local heat release rates compared to the simulation without Soret diffusion. To investigate this further, we compute flame elements by tracking the trajectories of reaction progress $c = Y_{H_2O}$ after interpolating the results onto a coarser mesh with $\Delta x/\delta_{th}^0 = \Delta y/\delta_{th}^0 = \Delta z/\delta_{th}^0 = 13$. Starting from a point on the flame iso-surface $Y_{H_2,iso}$, the trajectories are tracked in positive and negative ∇c-direction until a zero gradient of c is reached in both the burnt and unburnt gases. In terms of combustion modeling, these trajectories correspond to flamelets and describe the structure of the flame in composition space. The trajectories are depicted in Fig. 5 as red lines. The left half of each subfigure shows the temperature field, and the right half the local heat release rate, with the local enhancement at positively curved flame segments and local extinction at the negatively curved cusps.

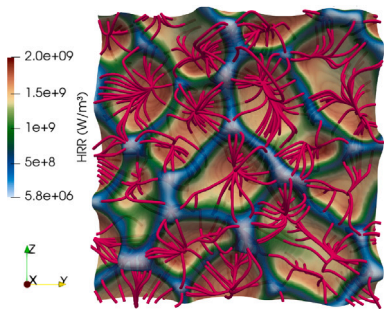

Fig. 6. Iso-surface of $Y_{H_2,iso}$ at $t/\tau = 7$ colored by HRR. Trajectories of c are shown as red lines.

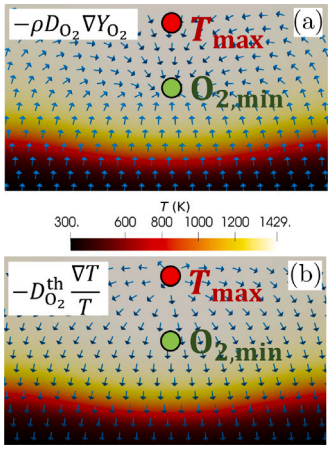

Fig. 7. Flame section from the red box in Fig. 5 showing the temperature field. Arrows indicate the direction of O_2 mass flux from Fick diffusion (top) and thermodiffusion (bottom).

Due to the defocused heat diffusion ($\nabla \cdot (-\lambda \nabla T) > 0$), where λ is the heat conductivity, and focused mass diffusion, super-adiabatic conditions ($T_{max} > T_{eq}$, where eq denotes chemical equilibrium) occur downstream of each positively curved flame segment. Since the flamelets follow ∇c, by definition, they all end at the super-adiabatic point behind each cell with $\nabla Y_{H_2O} = 0$. Note that the trajectories of c during the secondary cell formation are three-dimensional, as shown in Fig. 6 for a zoomed-in segment of the flame at $t/\tau = 7$.

As shown in Fig. 4, the curvature-induced variation of local equivalence ratio plays a crucial role in the heat release rates and thus propagation speeds. The diffusive mass flux of species k is computed from

$$\vec{j}_k = -\rho D_k \nabla Y_k - D_k^{th} \frac{\nabla T}{T}, \tag{2}$$

where D_k is the Fickian diffusion coefficient and D_k^{th} the thermodiffusion coefficient of the species. Fig. 5 at the top highlights a segment of the flame with a red box, which is shown in more detail in Fig. 7.

The diffusive mass flux of oxygen due to Fick diffusion is depicted in Fig. 7 at the top. As shown before, the focusing of the diffusive flux ($\nabla \cdot \vec{j}_{O_2} < 0$) leads to super-adiabatic conditions $Y_{O_2,max} > Y_{O_2,eq}$. For O_2, this means that downstream of each cell there is one point with the minimum O_2 mass fraction, marked with a green circle in Fig. 7. Since this is a minimum, the molecular flux due to Fickian diffusion is focused ($\nabla \cdot \vec{j}_{O_2} < 0$) on this point, as shown by the arrows in Fig. 7a. However, due to the strong Lewis number effect and thus the different focusing/defocusing of mass and heat fluxes, the point of maximum temperature is located downstream of the point of minimum Y_{O_2}, marked with a red circle in Fig. 7. Due to the positive thermal diffusion coefficient $D_{O_2}^{th} > 0$, the molecular O_2 flux due to

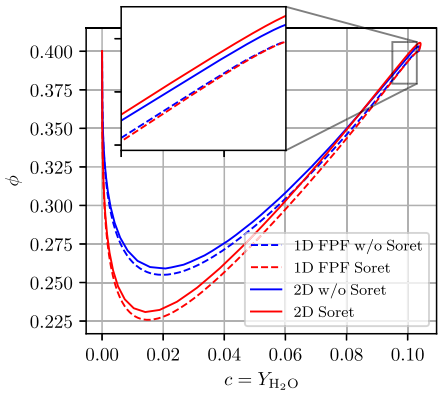

Fig. 8. ϕ along the trajectory of c passing through the maximum HRR of the flame at $t/\tau = 1.4$, shown for the 2D simulations with and without Soret diffusion as well as 1D reference flames.

thermodiffusion (Fig. 7b) points away from the point of maximum temperature, leading to defocusing of O_2 fluxes over a larger area. This is opposite to the mass flux of H radicals: due to the negative thermal diffusion coefficient ($D_H^{th} < 0$, $D_{O_2}^{th} > 0$), the thermodiffusive mass flux of H radicals is focused towards the point of max(T), while the point of min(Y_H) is located even further downstream of max(T), resulting in a less focused diffusive flux of H radicals from the flame front downstream. An extended version of Fig. 7 is provided as supplementary material.

The effect of these changed molecular fluxes is that local equivalence ratios for large values of c become higher when Soret diffusion is considered. This is in contrast to the 1D reference model flame at zero stretch, where max(T) and max(Y_{O_2}) are at the same location at $x \to \infty$. The flame structure is shown in Fig. 8 in terms of the trajectories of c, crossing the flame front at the point of maximum heat release for $t/\tau = 1.4$, showing the local equivalence ratio along the flamelet. At this time instance, the curvature of the flame front is still low and therefore the effect of Soret diffusion is not well pronounced. Nonetheless, the change in local equivalence ratio becomes visible. The dashed lines show the equivalence ratio along the 1D reference flames, blue lines show results without Soret diffusion and red lines with Soret diffusion. For the 1D reference flames, local equivalence ratios are strictly leaner throughout the whole flame for the simulation including Soret diffusion. For the trajectories crossing the positively curved flame segment in the 2D simulation (solid lines in Fig. 8), the same trend can be seen in the pre-heat zone of the flame. Towards $c > 0.8$, the local equivalence ratio of both the 2D simulations with and without Soret diffusion start to cross over, which is where most of the heat release occurs. For very high values of c, the local equivalence ratio exceeds the fresh gas mixture ϕ of 0.4, and the maximum of ϕ with Soret diffusion eventually exceeds the value predicted by flame without Soret diffusion.

At later time instances, where the cellular structures have grown and local curvatures increased, the influence of Soret diffusion becomes clearer. Fig. 9 shows 100 trajectories of the 3D simulation including Soret diffusion (blue lines, see also Fig. 6), the 2D simulation with Soret diffusion (red lines) and the 2D simulation without Soret diffusion (green lines, see also Fig. 5) each, which have been selected to all cross positively curved flame segments. Additionally, the dashed lines show the flame structure in terms of local equivalence ratio of the unstretched 1D reference flames with and without Soret diffusion.

For low values of c, the trend in the 2D simulations follows the 1D flame structure: Soret diffusion leads to lower values of ϕ compared with simulations without Soret diffusion along c. However, at larger values of c, this trend reverses and local equivalence ratios increase when the Soret diffusion is considered, leading ultimately to higher local heat release rates.

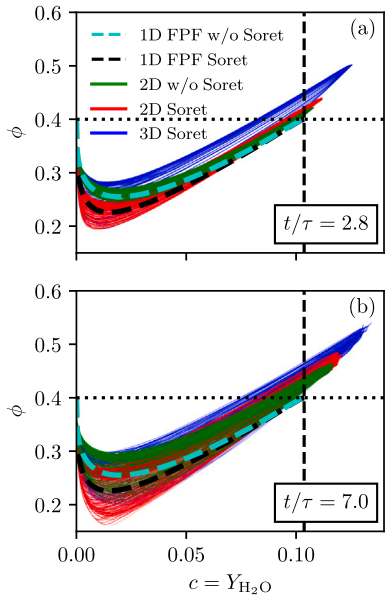

Fig. 9. Trajectories in $\phi - c$ space for the different simulation setups crossing positively curved flame segments.

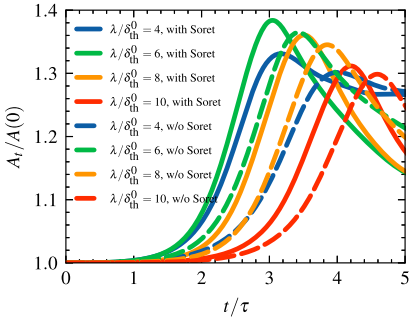

Fig. 10. Flame surface area over time for 2D simulations with (solid lines) and without (dashed lines) Soret diffusion for different initial perturbation wavelengths.

For the 3D simulations including Soret diffusion, the maximum local equivalence ratios exceed the ones from the 2D simulations due to the larger flame front curvatures in 3D. The vertical black dashed lines show the values of c at chemical equilibrium, showing that the super-adiabatic regions, especially in 3D, far exceed the fresh gas equivalence ratio of $\phi = 0.4$, as shown by the dotted black line. This also highlights the modeling challenge that the cellular instabilities present for lean hydrogen flames.

5. Wavelength-dependent impact of soret diffusion

To isolate the effect of perturbation wavelengths on the initial cell growth, additional 2D simulations have been performed where the domain height is adjusted to be $L_y = \lambda$ for each simulation. Fig. 10 shows the flame surface area from simulations with (solid lines) and without (dashed lines) Soret diffusion for different initial perturbation wavelengths λ. The most unstable wavelength is $\lambda \approx 6$ (which is in good agreement with the work by Berger et al. [2]) as shown by the fastest surface area growth rate. Including the Soret effect leads to a faster growth and larger peak surface area for all investigated wavelengths.

To assess the impact of Soret diffusion on the local propagation speeds, we evaluated the efficiency factor $I = (s_T/s_L^0)/(A_t/A_0)$, which represents a measure for the change in surface-averaged local burning

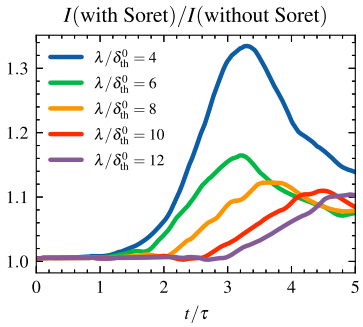

Fig. 11. Ratio of efficiency factors I with and without Soret diffusion over time for different initial perturbation wavelengths λ.

velocity. A_0 is the reference surface area given by the cross-section of the computational domain, and s_T is the integral flame speed

$$s_T = -\frac{1}{\rho_0 A_0 (Y^0_{H_2} - Y^b_{H_2})} \int \dot{\omega}_{H_2} \, \mathrm{d}V. \tag{3}$$

Here, ρ_0 is the density of the unburnt gas, $Y^0_{H_2}$ and $Y^b_{H_2}$ are the hydrogen mass fractions in the unburnt and burnt gas, respectively, and $\dot{\omega}_{H_2}$ is the reaction rate of hydrogen. Additional plots of I over time for selected perturbation wavelengths are provided in the supplementary material. In general, efficiency factors with Soret diffusion are higher compared to propagation where Soret diffusion is deactivated.

Interestingly, comparing the resulting efficiency factors with and without Soret diffusion does not result in a constant factor between them, but instead a dependence on the perturbation wavelength during earlier stages of cell growth has been found. Fig. 11 shows the ratio of efficiency factors with and without Soret diffusion during flame propagation and cell growth. The lower the initial perturbation wavelength, the larger the difference between efficiency factors with and without Soret diffusion. Lower perturbation wavelengths correspond to larger local curvatures, which in turn reinforce the focusing of diffusion fluxes. However, after the initial peak, the ratio of efficiency factors approaches 1.1 to 1.15 for the different perturbation wavelengths.

6. Global characteristics

So far, the difference of cell formation between the simulation setups were considered from a flame-local point-of-view. In this section, we consider the global characteristics of the flame evolution. In particular, Fig. 12a shows the relative flame surface area over time, where A_t is the instantaneous flame surface area and $A(0)$ the flame surface area at $t/\tau = 0$.

Comparing the change in flame surface area between the 3D simulation (blue line) and the 2D simulation including Soret diffusion (red line) shows that the surface area in 3D grows significantly faster. However, the time instance where the peak surface area of the primary cells is reached (first black vertical dashed line), as well as the time where the primary structures collapse to form the secondary structures (second vertical black line) remains the same. Running the simulation without Soret diffusion yields increases in surface area that are similar to the simulation with Soret diffusion, however, the peak surface area of the primary structures as well as the collapse into the secondary structures occurs later when Soret diffusion is not considered.

Since cellular instabilities still present a big challenge for modeling unstable hydrogen flames, e.g. in the context of large eddy simulations, the effect of the cellular structures has been evaluated in terms of the efficiency factor I. For a unity Lewis number flame, $I = 1$ and an increased propagation speed is caused only due to an increase in flame surface area. For lean hydrogen flames with $Le < 1$, local burning rates are increased at positively curved flame segments in general. Since most

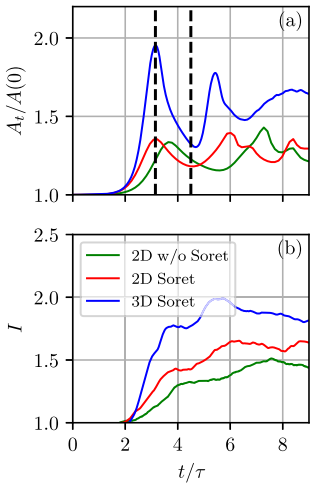

Fig. 12. Relative flame surface area (top) and efficiency factor I (bottom) over time for the different setups.

of the surface area of the flame with cellular instabilities is positively curved (negative curvature is only found in the small cusps), $I > 1$ is expected. The efficiency factor can therefore be considered as the effect of the structure of the cellular structures on the local chemistry, i.e. the enhancement of heat release rates and flame speeds.

The temporal evolution of I is depicted in Fig. 12b. While I for the 3D case is largest, followed by the 2D case including Soret diffusion, it is interesting to note that I is lower for the primary cells compared with the secondary cellular structure. This can also be seen in Fig. 4i, where local curvatures, both negative and positive, tend to have more extreme values than for the primary structures. Once the secondary structures have formed ($t/\tau > 6$), the value of I tends toward a constant value with an offset of about $\Delta I \approx 0.4$ between the 3D and 2D simulations. Therefore, using efficiency factors to describe the effect of (subgrid) cellular structures in combustion models might be feasible.

7. Summary and conclusions

Fully resolved simulations of the formation of cellular structures in a lean hydrogen–air flame at $\phi = 0.4$ were conducted, using a detailed reaction mechanism as well as detailed molecular diffusion. The flame is initially perturbed and the formation of primary as well as secondary structures is studied. Three different simulation setups are considered: (1) a 3D simulation including Soret diffusion, (2) a 2D simulation including Soret diffusion and (3) a 2D simulation without Soret diffusion. This allows the direct assessment of the effects of dimensionality and Soret diffusion on the flame structure and cell formation. The following conclusions have been drawn:

(i) Even at the same flame cross section in 2D, the additional principle curvature direction in 3D leads to higher local curvatures, leading to stronger focusing of diffusive fluxes, larger local equivalence ratios and thus higher heat release rates, that can exceed the maximum heat release rates from the 2D setup by 80%, leading to faster growth of flame surface area and propagation in 3D compared to 2D. However, the time at which the primary structures collapse is the same between 2D and 3D simulations.

(ii) For 1D unstretched flames, the inclusion of Soret diffusion leads to a slight decrease in laminar flame speed. However, in terms of cell formation from the thermodiffusive instability, Soret diffusion accelerates cell formation. Also, the transition from primary to secondary cells occurs earlier with Soret diffusion.

(iii) The inclusion of Soret diffusion leads to larger local equivalence ratios in the reaction and post-oxidation zone, which results in higher local heat release rates and thus propagation speeds. In the pre-heat zone, trends from the 1D freely propagating flames are unchanged, i.e. Soret diffusion leads to locally leaner conditions compared to simulations without Soret diffusion.

(iv) The efficiency factor I, quantifying the effect of the changed flame structure in the cells on the local chemistry, increases throughout the formation of the primary structures until the development of the secondary structures due to the generally more extreme values of curvature in the secondary structures. However, once the secondary structures are formed, the effect of the cells might be modeled with a constant value of I or a constant offset ΔI if simulations are performed in 2D or to capture the effects of cellular structures in the subgrid.

Novelty and significance statement

This work studies two important aspects of cell formation in thermodiffusively unstable hydrogen flames: dimensionality and Soret diffusion. In the literature, most numerical studies of cell formation in laminar flow configurations are limited to two-dimensional setups. This work quantifies the effect of running the simulations in 2D vs. 3D in terms of cell structure, flame propagation and global efficiency factor. The findings show that propagation speeds are significantly increased when running the simulation in 3D. efficiency factors are provided as a means to correct 2D simulation results. Additionally, this work assesses the effect of Soret diffusion on cell formation, which is found to accelerate the formation process. This is in contrast to the effect of Soret diffusion on flame speeds in 1D flames. An explanation is provided, which is the local increase of equivalence ratios in the reaction and post-oxidation zone of the flame.

CRediT authorship contribution statement

Thorsten Zirwes: Investigation, Visualization, Writing – original draft. **Feichi Zhang:** Resources, Conceptualization, Writing – review & editing. **Thomas L. Kaiser:** Investigation, Formal analysis, Writing – review & editing. **Kilian Oberleithner:** Investigation, Writing – review & editing. **Oliver T. Stein:** Investigation, Conceptualization, Writing – review & editing. **Henning Bockhorn:** Conceptualization, Supervision, Writing – review & editing. **Andreas Kronenburg:** Resources, Supervision, Writing – review & editing.

Declaration of competing interest

The authors declare that they have no known competing financial interests or personal relationships that could have appeared to influence the work reported in this paper.

Acknowledgments

Simulations were performed on the HoreKa supercomputer under the acronym dnsH2 funded by the Ministry of Science, Research and the Arts Baden-Württemberg and DFG (“Deutsche Forschungsgemeinschaft”). The authors gratefully acknowledge the financial support by the Helmholtz Association of German Research Centers (HGF), within the research field Energy, program Materials and Technologies for the Energy Transition (MTET), topic Resource and Energy Efficiency and the financial support by the Deutsche Forschungsgemeinschaft (DFG, project number 439610422).

Appendix A. Supplementary data

Additional data is available online.

Supplementary material related to this article can be found online at https://doi.org/10.1016/j.proci.2024.105665.

References

[1] L. Berger, A. Attili, H. Pitsch, Synergistic interactions of thermodiffusive instabilities and turbulence in lean hydrogen flames, Combust. Flame 244 (2022).
[2] L. Berger, A. Attili, H. Pitsch, Intrinsic instabilities in premixed hydrogen flames: Parametric variation of pressure, equivalence ratio, and temperature. Part 1-Dispersion relations in the linear regime, Combust. Flame 240 (2022) 111935.
[3] L. Berger, K. Kleinheinz, A. Attili, H. Pitsch, Characteristic patterns of thermodiffusively unstable premixed lean hydrogen flames, Proc. Combust. Inst. 37 (2019) 1879–1886.
[4] H. Lulic, A. Breicher, A. Scholtissek, P.E. Lapenna, A. Dreizler, F. Creta, C. Hasse, D. Geyer, F. Ferraro, On polyhedral structures of lean methane/hydrogen Bunsen flames: Combined experimental and numerical analysis, Proc. Combust. Inst. (2022).
[5] S. Shi, A. Breicher, J. Trabold, S. Hartl, R.S. Barlow, A. Dreizler, D. Geyer, Cellular structures of laminar lean premixed H2/CH4/air polyhedral flames, Appl. Energy Combust. Sci. 13 (2023).
[6] H. Böttler, H. Lulic, M. Steinhausen, X. Wen, C. Hasse, A. Scholtissek, Flamelet modeling of thermo-diffusively unstable hydrogen-air flames, Proc. Combust. Inst. (2022).
[7] C. Law, S. Ishizuka, P. Cho, On the opening of premixed bunsen flame tips, Combust. Sci. Technol. 28 (3–4) (1982) 89–96.
[8] T. Zirwes, F. Zhang, Y. Wang, P. Habisreuther, J.A. Denev, Z. Chen, H. Bockhorn, D. Trimis, In-situ flame particle tracking based on barycentric coordinates for studying local flame dynamics in pulsating bunsen flames, Proc. Combust. Inst. 38 (2021) 2057–2066.
[9] C.K. Law, G. Jomaas, J.K. Bechtold, Cellular instabilities of expanding hydrogen/propane spherical flames at elevated pressures: theory and experiment, Proc. Combust. Inst. 30 (1) (2005) 159–167.
[10] E. Hu, Z. Huang, J. He, J. Zheng, H. Miao, Measurements of laminar burning velocities and onset of cellular instabilities of methane–hydrogen–air flames at elevated pressures and temperatures, Int. J. Hydrog. Energy 34 (2009) 5574–5584.
[11] F. Zhang, T. Zirwes, Y. Wang, Z. Chen, H. Bockhorn, D. Trimis, D. Stapf, Dynamics of premixed hydrogen/air flames in unsteady flow, Phys. Fluids 34 (8) (2022).
[12] L. Berger, M. Grinberg, B. Jürgens, P.E. Lapenna, F. Creta, A. Attili, H. Pitsch, Flame fingers and interactions of hydrodynamic and thermodiffusive instabilities in laminar lean hydrogen flames, Proc. Combust. Inst. (ISSN: 1540-7489) 39 (2023) 1525–1534.
[13] J. Gaucherand, D. Laera, C. Schulze-Netzer, T. Poinsot, Intrinsic instabilities of hydrogen and hydrogen/ammonia premixed flames: Influence of equivalence ratio, fuel composition and pressure, Combust. Flame 256 (2023).
[14] X. Wen, T. Zirwes, A. Scholtissek, H. Böttler, F. Zhang, H. Bockhorn, C. Hasse, Flame structure analysis and composition space modeling of thermodiffusively unstable premixed hydrogen flames–Part I: Atmospheric pressure, Combust. Flame (2021).
[15] X. Wen, T. Zirwes, A. Scholtissek, H. Böttler, F. Zhang, H. Bockhorn, C. Hasse, Flame structure analysis and composition space modeling of thermodiffusively unstable premixed hydrogen flames–Part II: Elevated pressure, Combust. Flame (2021).
[16] S. Eckart, G. Pio, T. Zirwes, F. Zhang, E. Salzano, H. Krause, H. Bockhorn, Impact of carbon dioxide and nitrogen addition on the global structure of hydrogen flames, Fuel 335 (2022).
[17] K.R. Dinesh, H. Shalaby, K. Luo, J. van Oijen, D. Thévenin, Effects of pressure on cellular flame structure of high hydrogen content lean premixed syngas spherical flames: A DNS study, Int. J. Hydrog. Energy 41 (2016) 21516–21531.
[18] M. Rieth, A. Gruber, F.A. Williams, J.H. Chen, Enhanced burning rates in hydrogen-enriched turbulent premixed flames by diffusion of molecular and atomic hydrogen, Combust. Flame 239 (2022).
[19] T. Zirwes, F. Zhang, H. Bockhorn, Memory effects of local flame dynamics in turbulent premixed flames, Proc. Combust. Inst. 39 (2022) 2349–2358.
[20] A. Patyal, M. Matalon, Nonlinear development of hydrodynamically-unstable flames in three-dimensional laminar flows, Combust. Flame 195 (2018) 128–139.
[21] A. Patyal, M. Matalon, Isolating effects of Darrieus–Landau instability on the morphology and propagation of turbulent premixed flames, J. Fluid Mech. 940 (2022).
[22] A. Aspden, M. Day, J. Bell, Characterization of low Lewis number flames, Proc. Combust. Inst. 33 (1) (2011) 1463–1471.
[23] T. Howarth, E. Hunt, A. Aspden, Thermodiffusively-unstable lean premixed hydrogen flames: Phenomenology, empirical modelling, and thermal leading points, Combust. Flame 253 (2023) 112811.

[24] T. Howarth, A. Aspden, An empirical characteristic scaling model for freely-propagating lean premixed hydrogen flames, Combust. Flame 237 (2022) 111805.
[25] J.F. Grcar, J.B. Bell, M.S. Day, The Soret effect in naturally propagating, premixed, lean, hydrogen–air flames, Proc. Combust. Inst. 32 (1) (2009) 1173–1180.
[26] J. Schlup, G. Blanquart, Validation of a mixture-averaged thermal diffusion model for premixed lean hydrogen flames, Combust. Theory Model. 22 (2018) 264–290.
[27] T. Zirwes, M. Sontheimer, F. Zhang, A. Abdelsamie, F.E. Hérnandez Pérez, O.T. Stein, H.G. Im, A. Kronenburg, H. Bockhorn, Assessment of numerical accuracy and parallel performance of OpenFOAM and its reacting flow extension EBIdnsFoam, Flow Turbul. Combust. (2023).
[28] J. Li, Z. Zhao, A. Kazakov, F.L. Dryer, An updated comprehensive kinetic model of hydrogen combustion, Int. J. Chem. Kinet. 36 (2004) 566–575.
[29] R.J. Kee, M.E. Coltrin, P. Glarborg, Chemically Reacting Flow: Theory and Practice, John Wiley & Sons, 2005.